

Cite this: *Sustainable Energy Fuels*,  
2022, 6, 700

# Microstructured nitrogen-doped graphene-Sn composites as a negative electrode for high performance lithium-ion hybrid supercapacitors†

Miguel Granados-Moreno,<sup>1</sup> Gelines Moreno-Fernández,<sup>1\*</sup> Rosalía Cid,<sup>2</sup>  
Juan Luis Gómez-Urbano<sup>2,3</sup> and Daniel Carriazo<sup>1,4\*</sup>

Herein, we report a simplistic single-step synthesis of nitrogen-doped graphene decorated with tin particles suitable as a negative (battery-type) electrode for lithium-ion hybrid capacitors. An activated carbon derived from a graphene-carbon composite is used as a positive (capacitor-type) electrode. The excellent features of the nitrogen-doped graphene matrix combined with the homogeneous distribution and high theoretical capacity (994 mA h g<sup>-1</sup>) of the submicrometer-sized tin particles lead to an improved performance of the negative electrode, especially at high current densities. An optimized dual-carbon lithium-ion capacitor with 2 : 1 positive to negative mass ratio delivers high energy and power densities (133 W h kg<sup>-1</sup> at 142 W kg<sup>-1</sup> and 51 W h kg<sup>-1</sup> at 25 600 W kg<sup>-1</sup>). Furthermore, within a discharge time of 1 min, the device reaches 19 000 cycles with full capacity retention, delivering ca. 100 W h kg<sup>-1</sup> at 5600 W kg<sup>-1</sup>.

Received 8th November 2021  
Accepted 15th December 2021

DOI: 10.1039/d1se01779a

rsc.li/sustainable-energy

## 1. Introduction

In the few last decades, the research and development of new, safe and environmentally friendly energy storage devices has undergone important progress. This is of paramount importance for the implementation of a greener and circular economy with strong input from renewable energy sources. Until now, lithium-ion batteries (LIBs) showing large energy densities (~200 W h kg<sup>-1</sup>), low self-discharge and slow energy delivery have been the preferred choice for portable and cord-less applications.<sup>1,2</sup> On the other hand, supercapacitors (SC), delivering high power densities (>10 kW kg<sup>-1</sup>) and almost unlimited cycle life, dominate the market for high power applications such as start-stop systems in hybrid vehicles.<sup>3,4</sup> Obviously, there are still many applications, such as power backup in servers and storage devices, where the combination of high energy, power and long-term stability is required. In this sense, lithium-ion capacitors (LICs), comprising a battery-type and a capacitor-type electrode in the same cell, fill the gap between LIBs and SCs.<sup>5</sup> Briefly, in the battery-type electrode, usually the negative electrode, energy is stored by faradaic reactions due to Li<sup>+</sup> intercalation/de-intercalation in the bulk material. Conversely,

the capacitor-type electrode, usually the positive electrode, follows a capacitive mechanism where the charge is physically stored by fast adsorption/desorption of ions at the interface electrode/electrolyte. In this configuration, the battery-type electrode provides high capacity (high energy), while the capacitor-type enables a fast response (high power).<sup>6,7</sup>

Until now, graphite has been the most commonly used material for battery-type electrodes in LICs. Nevertheless, the sluggish intercalation of Li<sup>+</sup> hinders the performance at high power outputs.<sup>5,8</sup> Therefore, much effort has been made for the development of alternative materials showing higher capacities at faster rates of charge/discharge.<sup>9–11</sup> Metallic tin (Sn) is considered one of the most promising anode materials due to its large Li storage theoretical capacity (994 mA h g<sup>-1</sup>), low discharge potential *versus* Li/Li<sup>+</sup>, abundant resources and low price. Moreover, it is expected that Sn particles stabilize the electrode potential, protecting it from plating phenomena.<sup>12</sup> However, Sn suffers from large volume expansion during lithiation/de-lithiation (up to 300%) which leads to particle pulverization, structural fracture and loss of electrical contact.<sup>13–15</sup> As a result, Sn-based materials show fast capacity decay upon cycling. Moreover, alloy-type materials, such as tin, suffer from slow diffusion of Li<sup>+</sup> ions through the bulk material, hindering their performance at high rates. To overcome the aforementioned challenges, the encapsulation of Sn particles in a conductive framework has demonstrated to be a versatile approach, since it can not only promote fast electron transfer but can also buffer the volume changes taking place during charge/discharge. In this regard, nitrogen-doped graphene has been considered a promising candidate due to its bidimensional morphology that enables the wrapping of the small Sn

<sup>1</sup>Centre for Cooperative Research on Alternative Energies (CIC energiGUNE), Basque Research and Technology Alliance (BRTA), Alava Technology Park, Albert Einstein 48, 01510 Vitoria-Gasteiz, Spain. E-mail: mamoreno@cicenergigune.com; dcarriazo@cicenergigune.com; Tel: +34 94 529 71 08

<sup>2</sup>Universidad del País Vasco, UPV/EHU, 48080 Bilbao, Spain

<sup>3</sup>IKERBASQUE, Basque Foundation for Science, 48013 Bilbao, Spain

† Electronic supplementary information (ESI) available. See DOI: 10.1039/d1se01779a



particles. Moreover, nitrogen-doping induces topological defects that can offer extra lithium storage sites and enhances electronic conductivity increasing the capacity output even at fast charge/discharge rates.<sup>16–19</sup> This is of paramount importance in LIC technology, where the power performance is usually hindered by the slow kinetics of the battery-type electrode.

Regarding the capacitor-type electrode of LICs, carbonaceous materials showing large specific surface areas and wide pore size distribution are the preferred choice.<sup>8</sup> Among others, composites comprising activated carbon (AC) and graphene have demonstrated to enhance the charge storage capability.<sup>20</sup> Recently, we have reported a full optimized LIC using an activated carbon derived from the pyrolysis and activation of a graphene oxide–phenolic resin composite (ResFaGO-A) as a capacitive electrode.<sup>21</sup> The presence of graphene not only increased the surface area of the material, but also improved the electronic conductivity, maximizing the capacitance at high power rates. With this configuration, we reached a power density of 26 000 W kg<sup>-1</sup> with excellent cycling performance. However, the maximum energy stored (91 W h kg<sup>-1</sup>) can be highly improved. Therefore, knowing that ResFaGO-A shows an excellent performance at high rates it seems reasonable to use it as a capacitor-type material and replace the battery-electrode with another higher capacity one.

In this work, we have developed a graphene-based dual carbon LIC comprising our previously reported activated carbon–graphene composite (ResFaGO-A) as a capacitive electrode. The battery material nitrogen-doped reduced graphene oxide decorated with Sn particles (rGO800-N-Sn) was developed by an easy scalable and novel one-step synthesis. It was found that the presence of Sn in the negative electrode enhances the capacitive performance of LICs, at the time that prevents plating phenomena. Optimized LICs deliver high energy and power densities of 133 W h kg<sup>-1</sup> at 142 W kg<sup>-1</sup> and 51 W h kg<sup>-1</sup> at its maximum power output (25 600 W kg<sup>-1</sup>). Moreover, this LIC showed an outstanding cycling performance, retaining 100% of its initial capacitance after 19 000 cycles.

## 2. Experimental

### 2.1. Synthesis of rGO800-N-Sn, rGO800-N and ResFaGO-A

Nitrogen-doped reduced graphene oxide decorated with tin particles (thereafter denoted as rGO800-N-Sn) was obtained by adding 100 mg of SnSO<sub>4</sub> (Sigma-Aldrich, ≥95%) and 100 mg of sucrose (Sigma-Aldrich, ≥99.0%) to 50 mL of an aqueous solution of commercial graphene oxide (Graphenea, 4 mg mL<sup>-1</sup>). The mixture was homogenized using a magnetic stirrer for 1 h and then, the dispersion was freeze-dried for 3 days. The resulting dry powder was ground with melamine (Sigma-Aldrich, 99%) at a mass ratio of 1 : 1. The mixture was subsequently treated in a tubular oven at 800 °C for 1 h under a dynamic argon atmosphere to obtain the final material. For the sake of comparison, nitrogen-doped reduced graphene oxide (thereafter denoted as rGO800-N) was synthesized following the same procedure but in the absence of SnSO<sub>4</sub> and sucrose.

The activated carbon, ResFaGO-A, was prepared following our previously reported method.<sup>21</sup> Briefly, 440 mg of resorcinol (Sigma-Aldrich, 99%) were dissolved in 4.0 mL of water, 2.4 mL of ethanol and 4.0 mL of graphene oxide (Graphenea, 4 mg mL<sup>-1</sup>). After complete dissolution of resorcinol, 600 μL of formaldehyde (Sigma-Aldrich, 37% w/w in H<sub>2</sub>O containing 10–15% methanol) and 100 μL of concentrated phosphoric acid (Sigma-Aldrich, ≥85% w/w in H<sub>2</sub>O) were rapidly added to the suspension. The mixture was transferred to a closed container and heated in an oven at 85 °C for 70 h. Resulting resins were pre-carbonized at 800 °C in a tubular oven for 1 h under a dynamic Ar atmosphere. Then, carbon was ground together with KOH (Sigma-Aldrich, ≥85%) at a C : KOH mass ratio of 1 : 6 and further carbonized in a tubular oven at 800 °C for 1 h under a dynamic Ar atmosphere. The resulting material was washed once with diluted HCl and then several times with hot deionized water to obtain ResFaGO-A.

### 2.2. Physicochemical characterization

Morphological characterization was performed by scanning electron microscopy (SEM) in a Quanta200 FEI (3 kV, 30 kV) microscope. Additional morphological information was obtained by transmission electron microscopy (TEM) in a FEI – TECNAI G2 F20 S-TWIN microscope at an acceleration voltage of 200 kV and a spot size of 3. The microstructure of the samples was analyzed by X-ray diffraction (XRD) in a Bruker D8 X-ray diffractometer. Data were collected using Cu K $\alpha$  radiation within the  $2\theta$  range from 10° to 80° at steps of 0.02° and a residence time of 2 s. Raman spectra were recorded with a Renishaw spectrometer (Nanoionics Multiview 2000) operating with an excitation wavelength of 532 nm. Nitrogen adsorption–desorption isotherms were obtained at –196 °C using an ASAP 2460 instrument from Micromeritics. Samples were outgassed at 150 °C for 12 h under vacuum prior to the analysis. The specific surface area ( $S_{\text{BET}}$ ) values were calculated using the Brunauer–Emmett–Teller (BET) equation in the relative pressure range between 0.05 and 0.25. The pore size distributions were calculated using the 2D-NLDFT model applied from the data of the adsorption branches using the SAIEUS software. X-ray Photoelectron Spectra were recorded using a Phoibos 150 XPS spectrometer (SPECS Surface Nano Analysis) installed in a UHV chamber with a base pressure of 10<sup>-10</sup> mbar. All spectra were collected in Fixed Analyzer Transmission (FAT) mode using a field of view on the sample around 2 mm with a non-monochromatic Mg K $\alpha$  source.  $E_{\text{step}} = 0.5$  eV and  $E_{\text{pass}} = 60$  eV were used for survey spectra, while  $E_{\text{step}} = 0.1$  eV and  $E_{\text{pass}} = 30$  eV were employed for the high-resolution regions of the different elements. Elemental analysis (EA) measurements were carried out in a Flash 2000 Thermo Scientific CHNS–O for the rGO800-N-Sn and rGO800-N samples to analyze the bulk content of each element. The tin amount in the samples was determined by inductively coupled plasma spectroscopy (ICP). Samples were analyzed using a Horiba Ultima 2 (Jobin Yvon) in conjunction with an AS500 autosampler and Activanalyzer software (version 5.4). The ICP-OES operating conditions were as follows: 1.0 kW RF power, 13 L min<sup>-1</sup> plasma-gas flow rate, 0.2 L min<sup>-1</sup> sheath-gas flow rate and 0.25 L min<sup>-1</sup> nebulizer-gas flow



rate. Solutions were introduced into the plasma torch using a nebulizer and a cyclonic type spray chamber at a flow rate of  $0.87 \text{ mL min}^{-1}$ . Calibration solutions were prepared using a commercial calibration standard of Sn (Scharlab) at concentration of  $1000 \text{ mg L}^{-1}$ . Ultrapure Water (Fischer Scientific) was used for dilution.

### 2.3. Electrochemical characterization

Both negative (rGO800-N and rGO800-N-Sn) and positive (ResFaGO-A) electrodes were processed by mixing the active materials together with super P C-65 conductive carbon and a polyvinylidene fluoride (PVDF) binder in a 90 : 5 : 5 mass ratio using *N*-methyl-2-pyrrolidone (NMP) as solvent. NMP-Based inks of negative and positive electrodes were coated on copper and aluminum foil, respectively. Laminates were dried at  $80 \text{ }^\circ\text{C}$  under vacuum overnight. Electrode discs of 12 mm were further punched out from the laminates and dried at  $120 \text{ }^\circ\text{C}$  overnight under vacuum prior to cell assembly.

rGO800-N ( $1 \pm 0.5 \text{ mg}$ ,  $0.06 \pm 0.01 \text{ mm}$ ) and rGO800-N-Sn ( $1 \pm 0.5 \text{ mg}$ ,  $0.02 \pm 0.01 \text{ mm}$ ) electrodes were firstly evaluated in two-electrode Swagelok-type cells using a half cell configuration with a metallic lithium disc as the counter and reference electrode. Galvanostatic charge/discharge measurements were carried out at different C-rates (being 1C:  $372 \text{ mA h g}^{-1}$  according to the theoretical capacity of graphite) between 0.002 and 2.0 V vs. Li/Li<sup>+</sup>.

Battery-type electrodes were pre-lithiated before LIC cell assembly. For this purpose, two-electrode Swagelok-type cells were assembled using a lithium metal disc as the counter and reference electrode. The pre-lithiation process involved 5 charge/discharge cycles at C/10 between 0.002 and 2.0 V vs. Li/Li<sup>+</sup> followed by a final discharge at C/40 to 0.2 V vs. Li/Li<sup>+</sup>. Then, LIC cells were assembled in a three-electrode Swagelok cell using pre-lithiated rGO800-N or rGO800-N-Sn as the negative electrode, ResFaGO-A as the positive electrode and a metallic lithium disc as the reference electrode. Positive/negative electrode mass ratios of LIC 2 : 1 ( $2 \pm 0.5 \text{ mg cm}^{-2}$  :  $1 \pm 0.5 \text{ mg cm}^{-2}$ ) and LIC 1 : 1 ( $1 \pm 0.5 \text{ mg cm}^{-2}$  :  $1 \pm 0.5 \text{ mg cm}^{-2}$ ) were evaluated. The negative electrode potential was set to 0.2 V vs. Li/Li<sup>+</sup> and the positive electrode potential to 4.2 V vs. Li/Li<sup>+</sup>. Galvanostatic charge/discharge measurements for the LICs were performed within the 1.5–4.2 V voltage range at different current densities. Whatman D-type glass fibers discs of 13 mm in diameter and 1 M lithium hexafluorophosphate (LiPF<sub>6</sub>) in 1 : 1 v/v of ethylene carbonate (EC) and dimethyl carbonate (DMC) were used as a separator and electrolyte, respectively in all the measurements. Specific capacity and current density values were calculated with respect to the total mass of active material. Measurements were conducted using a multichannel VMP3 generator (Biologic).

## 3. Results and discussion

### 3.1. Battery-type electrode characterization

As commented previously, a composite comprising tin particles encapsulated in a N-doped graphene matrix (rGO800-N-Sn) was

synthesized and evaluated as a battery-type electrode for its further assembly into a LIC full cell. Due to the aforementioned challenges associated with the use of tin as an anode material (slow diffusion of Li<sup>+</sup> ions and large volume changes), expensive and time consuming synthesis routes are commonly followed to guarantee good performance at high current densities and preserve the lifetime.<sup>22,23</sup> Herein, rGO800-N-Sn was obtained by an easy one step of carbonization at  $800 \text{ }^\circ\text{C}$ . During thermal treatment, several key processes take place simultaneously. First, the thermal treatment leads to partial removal of the oxygenated functional groups present in the GO structure, partially restoring its sp<sup>2</sup> graphitic characteristics with subsequent improvement of its electronic conductivity. Second, at high temperatures, nitrogen atoms produced from the decomposition of melamine are introduced in the graphene-based network, yielding a nitrogen functionalized material. Third, between 200 and  $400 \text{ }^\circ\text{C}$  SnSO<sub>4</sub> is converted to SnO<sub>2</sub> along with the release of SO<sub>2</sub> gas. Further, at ca.  $600 \text{ }^\circ\text{C}$  the as-formed SnO<sub>2</sub> is reduced in the presence of carbon to metallic tin particles, which are homogeneously deposited in the N-rGO based matrix. Fourth, carbon derived from sucrose decomposition is deposited on top of the particles, which together with the graphene matrix helps buffer the volume changes and enables fast charge transfer. Additionally, to properly evaluate the influence of tin particles in the composite, a sample was synthesized in the absence of SnSO<sub>4</sub> and sucrose (rGO800-N).

The materials were analyzed by elemental analysis and ICP to determine their composition. Table 1 shows that 28.6% of the mass of rGO800-N-Sn corresponds to metallic Sn, 63% to carbon, 3.9% to oxygen and 3.3% to nitrogen. A similar nitrogen doping amount of 2.1% was also found for the rGO800-N sample, but the oxygen content was considerably higher 24.3%. This can be explained by the partial substitution of oxygen atoms in the graphitic matrix by Sn particles for rGO800-N-Sn.

The morphologies and microstructures of rGO800-N and rGO800-N-Sn were evaluated by SEM imaging. As displayed in Fig. 1 both materials show a highly opened 3D macroporous conducting network composed of N-graphene sheets. The successful incorporation of tin into the rGO800-N-Sn composite is evidenced in Fig. 1b and d. It is worth mentioning that Sn particles are homogeneously embedded into the N-graphene matrix with a submicrometer particle size ranging from 0.2 to  $1 \text{ }\mu\text{m}$ . TEM images of the rGO800-N-Sn sample further confirm the homogenous distribution of spherically shaped tin particles embedded within the graphene sheets (Fig. S1a†). Moreover,

Table 1 Elemental composition of the as-synthesized battery-type materials

	C <sup>a</sup> (wt%)	N <sup>a</sup> (wt%)	Sn <sup>b</sup> (wt%)	O <sup>c</sup> (wt%)
rGO800-N	72.5	2.1	—	24.3
rGO800-N-Sn	63.0	3.3	28.6	3.9

<sup>a</sup> Carbon and nitrogen bulk content determined by elemental analysis.

<sup>b</sup> Tin bulk content determined by ICP. <sup>c</sup> Oxygen bulk content determined by difference.



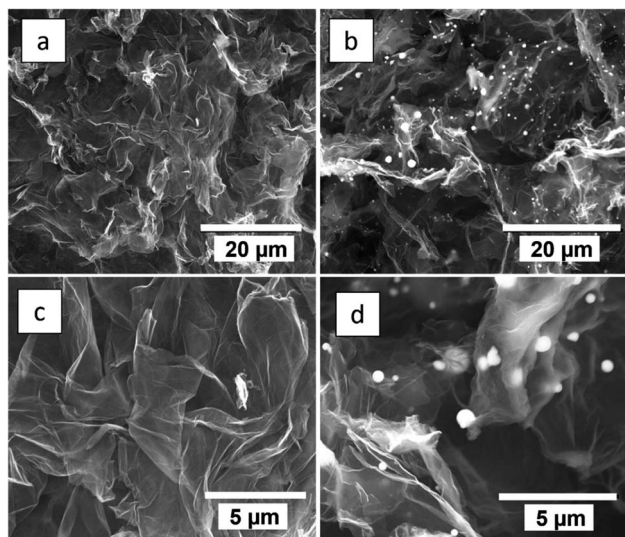


Fig. 1 SEM images of rGO800-N (a and c) and rGO800-N-Sn (b and d).

irregular-shaped tin particles with a size below 1  $\mu\text{m}$  are also observed at higher magnifications (Fig. S2b†). It is expected that the reduced particle size provides a better electrochemical

performance due to several factors. First, electronic contact between the matrix and Sn particles is improved considerably with the consequent increase of conductivity, leading to higher capacity values. Second, a decrease of Sn particle size entails shortening of the diffusion pathways, which leads to beneficial results in terms of high current density behavior. Third, the sub-micrometer particle size leads to better coverage by the conductive matrix, allowing better buffering of the volume changes taking place during charge/discharge.<sup>14,24</sup>

Battery-type materials were subjected to X-ray diffraction to gain structural information as can be seen in Fig. 2a. Both samples show low-intensity broad bands at *ca.*  $28^\circ$ , which can be indexed to the C(002) reflection corresponding to basal diffractions of graphite, pointing out that a certain restacking of the graphene layers has taken place in thermally reduced graphene oxides. The appearance of several intense and sharp peaks in the rGO800-N-Sn diffractogram confirms the presence of crystalline metallic tin in the composite (JCPDS 04-0673).<sup>25,26</sup>

The Raman spectra of both rGO800-N and rGO800-N-Sn materials were recorded and deconvoluted as illustrated in Fig. 2b. Both spectra show broad peaks at *ca.*  $1355\text{ cm}^{-1}$  and  $1595\text{ cm}^{-1}$  assigned to the D and G bands of carbons, respectively. The D-band is related to the presence of dispersive defect induced vibrations while the G-band is associated with the

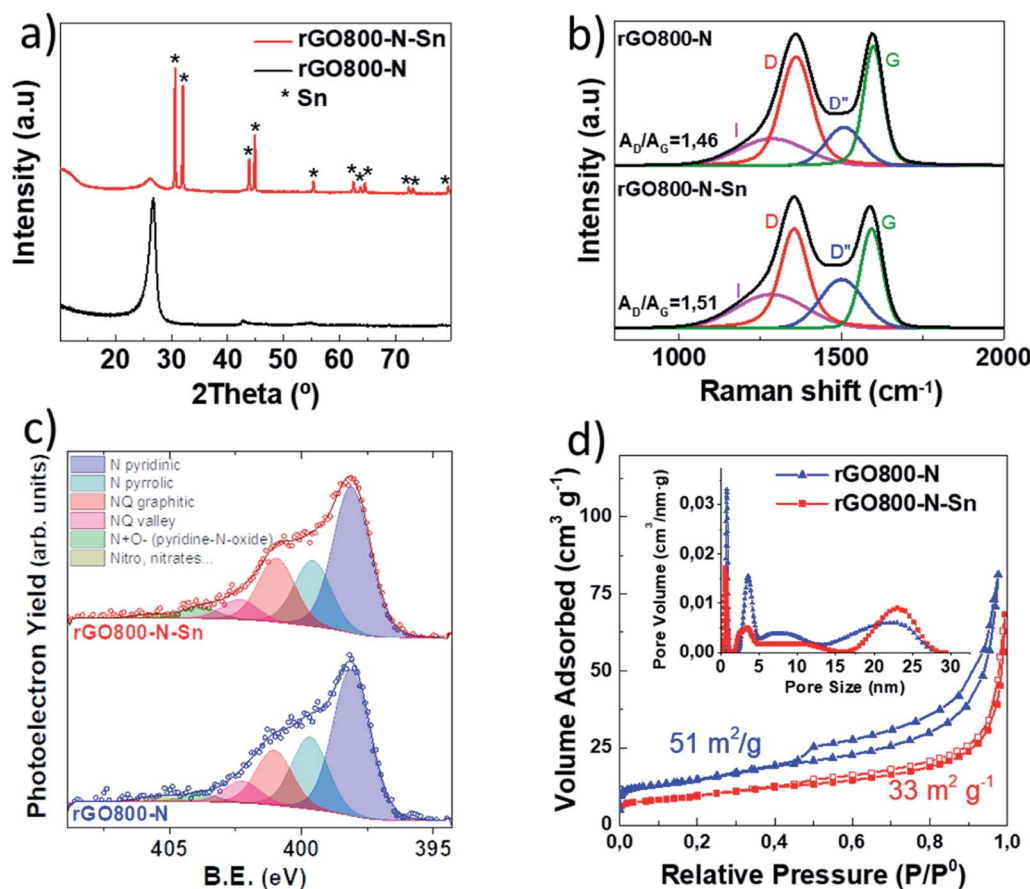


Fig. 2 XRD spectra (a), Raman spectra (b), high-resolution XPS spectra for N 1s (c) and adsorption/desorption isotherms and pore size distribution of (d) registered rGO800-N-Sn and rGO800-N samples.



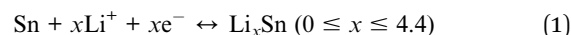
vibrations of ordered graphitic domains. The larger  $A_D/A_G$  ratio measured for the rGO800-N-Sn powder (1.51) compared to the rGO800-N one (1.46) indicates a slightly higher number of defects in the structure of the tin containing sample. The fitted I band at *ca.* 1275  $\text{cm}^{-1}$  and the  $D''$  band at *ca.* 1500  $\text{cm}^{-1}$  are related to the disorder in the graphitic lattice and the presence of amorphous phases. The slightly bigger  $D''$  band fitted for rGO800-N-Sn can be ascribed to the amorphous carbon product from sucrose decomposition during thermal treatment.<sup>27,28</sup>

These observations are in agreement with the XPS results, since the fitting of  $C_{1s}$  spectra also shows a higher graphitic characteristic for the rGO800-N sample (see Fig. S2†). This is evidenced by the higher proportion of component  $C_1$  (59.1% in rGO800-N *vs.* 56.5% in rGO800-N-Sn) representing the graphitic C–C  $sp^2$  signal, as well as the reduced  $C_2/C_1$  quotient (0.26 *vs.* 0.40), where component  $C_2$  accounts for the aliphatic C–C  $sp_3$  signal, and defects in the graphitic lattice.<sup>29</sup> Nevertheless, it may also contain some C–N bonds and  $sp^2$  C–C in the close vicinity of N or O atoms.<sup>30,31</sup> On the other hand,  $N_{1s}$  spectra reveal a broad peak, indicating the formation of multiple functional groups. The unambiguous assignment to specific nitrogen species is not straightforward since many of them overlap significantly. Pyridinic, pyrrolic and quaternary nitrogen functionalities are commonly found in nitrogen doped carbons. We can easily deconvolute the  $N_{1s}$  spectra into 6 components peaking at energies of 398.1 eV ( $N_1$ ), 399.6 eV ( $N_2$ ), 400.9 eV ( $N_3$ ), 402.2 eV ( $N_4$ ), 403.8 eV ( $N_5$ ) and 405.6 eV ( $N_6$ ).  $N_1$  and  $N_2$  can be assigned to pyridinic and pyrrolic N respectively, while  $N_3$  and  $N_4$  are attributed to graphitic-like quaternary N occupying central positions (inside an intact graphene region) and valley positions (neighboring a defect site) in the lattice.<sup>30,31</sup> Finally,  $N_5$  and  $N_6$  correspond to oxidized N, with  $N_5$  ascribed to pyridine-N-oxide and  $N_6$  to other oxide functionalities such as nitro groups and nitrates as well as chemisorbed N.<sup>32</sup> It has been previously reported that not all the N functionalities have the same impact for lithium storage.<sup>33</sup> The improved performance of nitrogen-doped carbon materials arises from a large pyridinic proportion, which is the main functionality of both as-synthesized materials (Table 2). Pyridinic N can create individual or triple vacancies in a plane of graphitic framework to enhance the reversible capacity and the rate capability.<sup>33–35</sup>

The textural properties of rGO800-N and rGO800-N-Sn samples were investigated by  $N_2$  adsorption/desorption (Fig. 2d). Both samples display mixed type II and IV isotherms with a H3-type hysteresis loop, characteristic of meso–macroporous materials.<sup>36</sup> As a consequence of the addition of non-porous tin particles,  $S_{BET}$  decreases from 51  $\text{m}^2 \text{g}^{-1}$  for rGO800-N to 33  $\text{m}^2 \text{g}^{-1}$  for rGO800-N-Sn. The pore size distribution ranges between 4 and 28 nm pointing to the mesoporous

nature of both materials. Also, the presence of Sn leads to the depletion of smaller mesopores accompanied by the evolution of larger ones. This is expected to ensure efficient diffusion of  $\text{Li}^+$  and provide abundant accommodation space for Sn growth.<sup>18</sup>

The electrochemical performances of rGO800-N and rGO800-N-Sn were preliminarily evaluated in a half-cell configuration by cycling at several current densities from 0.002–2.0 V *vs.*  $\text{Li}/\text{Li}^+$ . Galvanostatic charge/discharge curves at different rates after 5 stabilization cycles are shown in Fig. 3a and b for rGO800-N and rGO800-N-Sn, respectively. In the case of rGO800-N, typical sloping profiles characteristic of  $\text{Li}^+$  insertion in non-graphitic carbons are observed. On the other hand, rGO800-N-Sn shows marked plateaus corresponding to Sn–Li alloying at voltages below 0.8 V.<sup>15,19,21</sup> For a better understanding Fig. 3c shows a comparison of the differential capacity plots ( $dQ/dV$ ) obtained for both materials. During discharge, gradual alloying of Sn particles to  $\text{Li}_x\text{Sn}$ , is evidenced at 0.67, 0.64 and 0.4 V for rGO800-N-Sn. Afterwards, three peaks can be identified at 0.58, 0.71, and 0.79 V in the charge branch ascribed to the dealloying reaction of  $\text{Li}_x\text{Sn}$  to metallic Sn.<sup>18,22</sup> These oxidation and reduction peaks are assigned to reversible processes following eqn (1).



These alloying/dealloying reactions of tin with lithium improve the capacity of the rGO800-N-Sn composite in the whole current density range compared to the pristine sample (Fig. 3d). In fact, 476, 407, 357, 319, 275, 188 and 120  $\text{mA h g}^{-1}$  are delivered at current rates of C/10, C/5, C/2, C, 2C, 5C and 10C, with a coulombic efficiency (CE) close to 100% after six stabilization cycles. On the other hand, only 366, 273, 207, 158, 114, 66 and 41  $\text{mA h g}^{-1}$  are provided by rGO800-N at similar current rates. Regarding the first cycle CE (Fig. S3†), the Sn-containing material shows a slightly lower value (43 *vs.* 50%) due to the hindered formation of the stable SEI.<sup>37</sup> This phenomenon previously reported for tin-based materials has been ascribed to the large number of  $\text{Li}^+$  ions that are irreversibly trapped during the first lithiation process. In our case this can be due to extraction/diffusion limitations in large Sn particles, and also the presence of a very thin oxide layer on the surface of the metallic Sn particles, with which lithium ions irreversibly react contributing to the SEI formation. Nevertheless, thanks to its low surface area combined with the good encapsulation of submicrometer-sized tin particles into the mesoporous N-graphene matrix, the coulombic efficiency is highly improved in the second cycle. In addition, the presence

Table 2 Nitrogen species determined by XPS of the as synthesized battery-type materials

	N pyridinic (%)	N pyrrolic (%)	NQ graphitic (%)	NQ valley (%)	Pyridine-N-oxide (%)	Other N oxides (%)
rGO800-N	47.2	23.4	17.9	7.1	2.6	1.8
rGO800-N-Sn	46.7	21.2	20.6	6.5	3.7	1.3



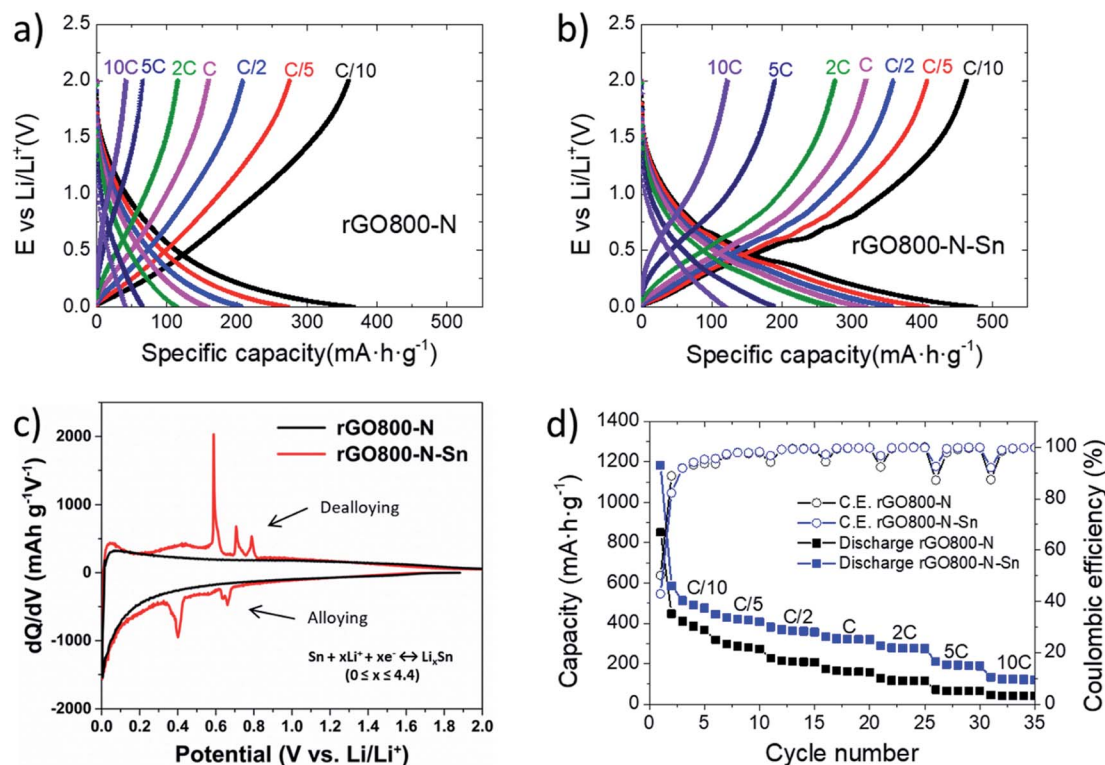


Fig. 3 Electrochemical characterization of the battery-type electrodes: galvanostatic charge/discharge curves at different current rates for rGO800-N (a) and rGO800-N-Sn (b), differential capacity vs. voltage plot (c) and rate capability and their respective coulombic efficiency (d).

of nitrogen heteroatoms at the edge-plane sites minimizes the number of irreversible trapped lithium ions.<sup>18,38</sup>

### 3.2. Capacitor-type electrode characterization

In our previous work we already reported the characterization of a capacitor-type material for the positive electrode of a LIC.<sup>21</sup> Briefly, ResFaGO-A is an activated carbon prepared by KOH activation of a phenolic resin/graphene composite. The flat-shape morphology within the large surface area (2318 m<sup>2</sup> g<sup>-1</sup>) and wide pore size distribution allowed a high specific capacitance of 181 F g<sup>-1</sup> (136 mA h g<sup>-1</sup>) at 0.25 A g<sup>-1</sup> and excellent capacitance retention of 84 F g<sup>-1</sup> (60 mA h g<sup>-1</sup>) at 40 A g<sup>-1</sup> when measured at 1.5–4.2 V vs. Li/Li<sup>+</sup> in a three electrode-cell configuration.

### 3.3. Lithium-ion capacitor

As has been explained above, ResFaGO-A was selected for the positive (capacitor-type) electrode while rGO800-N and rGO800-N-Sn were both evaluated as negative (battery-type) electrodes to study the impact of Sn on the LIC performance. Prior to LIC assembly rGO800-N and rGO800-N-Sn were pre-lithiated to form the SEI and supply enough lithium to balance the first cycle irreversibility.<sup>39</sup> Briefly, electrodes were cycled between 0.002 and 2 V vs. Li/Li<sup>+</sup> at C/10 using an auxiliary Li electrode. Then, a cut-off potential of 0.2 V vs. Li/Li<sup>+</sup> was set to maximize the use of the negative electrode and prevent lithium plating. In order to maximize the output capacity, mass balance of the electrodes

was performed. The charge stored in each electrode must be equal  $Q_+ = Q_-$  and it is directly proportional to the specific capacity ( $C_+$ ,  $C_-$ ) and the working potential window ( $\Delta E_+$ ,  $\Delta E_-$ ).<sup>40</sup>

$$Q_+ = m_+ C_+ \Delta E_+ \quad (2)$$

$$Q_- = m_- C_- \Delta E_- \quad (3)$$

Nevertheless, it must be considered that the working potential window in the final LIC differs from the one used to electrochemically characterize both electrodes individually. Fig. S4† shows that the specific capacities of rGO800-N and rGO800-N-Sn converge with that of ResFaGO-A at current densities of 0.8 and 6 A g<sup>-1</sup>, respectively, which makes it difficult to select an appropriate mass balance that suits for both materials. With this regard, a mass balance of 1 : 1 (LIC 1 : 1) was firstly selected for the comparison of both systems.

LICs were galvanostatically cycled at different current densities in the cell voltage range 1.5–4.2 V. At 0.1 A g<sup>-1</sup> (Fig. 4a and c) both LICs 1 : 1 show symmetric profiles with a linear voltage dependence characteristic of capacitive storage with an almost unappreciable ohmic drop.<sup>5</sup> It can be observed that for LIC full cells including rGO800-N (discharge time of 26 min), the positive electrode fluctuates from 2.40 to 4.37 V (1.97 V) and the negative from 0.89 to 0.17 V (0.72 V). Similarly, the positive electrode of a rGO800-N-Sn based LIC (discharge time of 28 min) swings from 2.41 to 4.54 V (2.13 V) and the negative from 0.9 to 0.35 V (0.55 V). The evolution of the alloying/dealloying



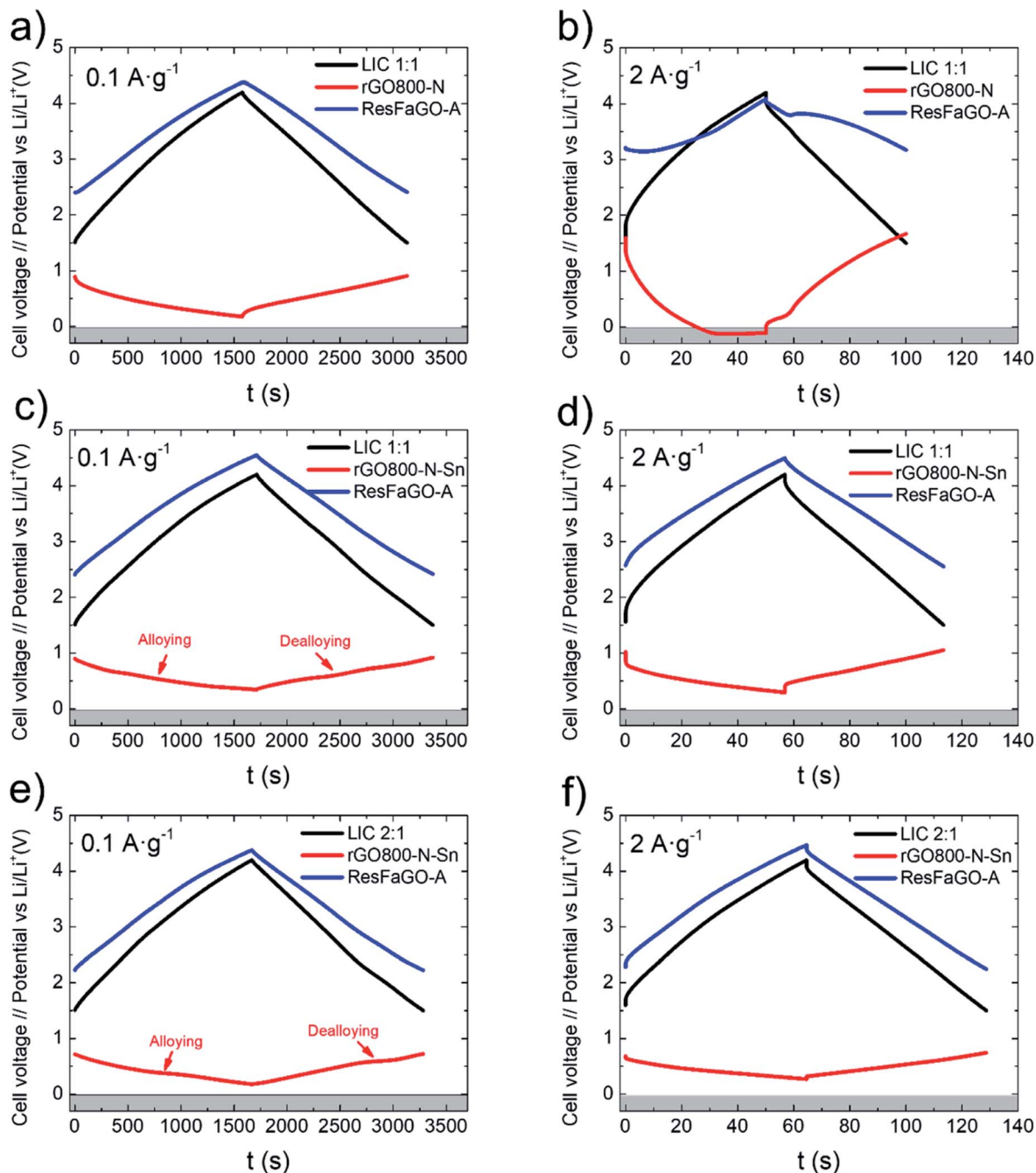


Fig. 4 Galvanostatic charge/discharge profiles at 0.1 and 2 A g<sup>-1</sup> for: LIC1:1\_rGO800-N (a and b) LIC1:1\_rGO800-N-Sn (c and d) and LIC2:1\_rGO800-N-Sn (e and f); LIC (black), the negative electrode (red) and the positive electrode (blue).

plateaus in the negative electrode profile of the tin-containing LIC is also worth mentioning.<sup>15</sup>

When the current density is increased to 2 A g<sup>-1</sup> (Fig. 4b and d), the rGO800-N based LIC (discharge time of 50 s) shows distorted profiles with an appreciable ohmic drop. The positive electrode swings from 3.21 to 4.11 V (0.9 V). On the other hand, the negative electrode goes from 1.61 to -0.11 V (1.72 V), reaching negative values and thus leading to lithium plating, which can compromise the safety of the cell.<sup>41</sup> On the other hand, the rGO800-N-Sn based LIC at 2 A g<sup>-1</sup> (discharge time of

56 s) shows sloping profiles and a very low ohmic drop. The positive electrode fluctuates from 2.57 to 4.49 V (1.92 V) and the negative from 1.02 to 0.29 V (0.73 V). It is worth highlighting that even when the current density is increased up to 10 A g<sup>-1</sup> this LIC is protected from lithium plating, ensuring a safe operation (Fig. S5a†).

In view of the results and the aim to maximize the output capacity of the rGO800-N-Sn negative electrode, a LIC with a mass balance 2 : 1 positive to negative was assembled. Fig. 4e shows that for a current density of 0.1 A g<sup>-1</sup>, the positive



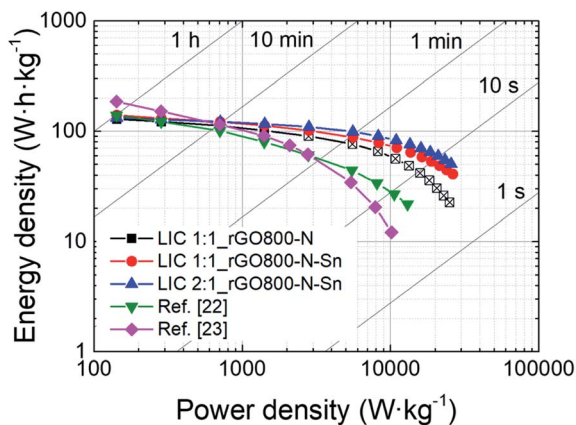


Fig. 5 Ragone plot comparing the gravimetric energy and power densities of LIC 1:1\_rGO800-N, LIC 1:1\_rGO800-N-Sn, LIC 2:1\_rGO800-N-Sn and previous studies (ref. 22 and 23). Open black squares correspond to stages that can undergo lithium plating.

electrode of rGO800-N-Sn based LIC2:1 (discharge time of 27 min) fluctuates from 2.22 to 4.37 V (2.15 V) and the negative from 0.72 to 0.18 (0.54 V). Herein, the alloying/dealloying plateaus are even more pronounced confirming the maximized capacity output. When the current density is increased to  $2 \text{ A g}^{-1}$  (Fig. 4f), with a discharge time of 64 s, the positive electrode works between 2.28 and 4.47 V (2.19 V) and the negative between 0.68 and 0.27 V (0.41 V). Again, it seems that the incorporation of Sn into the N-graphene matrix prevents lithium plating by offering additional lithiation sites. Even at a high current density of  $10 \text{ A g}^{-1}$ , the negative electrode is kept

well above 0 V in this LIC2:1, preventing lithium plating and ensuring safe operation (Fig. S5b†).

Fig. 5 shows the comparison of the energy and power performances of the three different LICs calculated from the galvanostatic curves in the voltage range 1.5–4.2 V. It is clearly shown that at low power densities the three systems deliver similar energy densities ( $\sim 133 \text{ W h kg}^{-1}$ ), but at high power rates ( $3000 \text{ W kg}^{-1}$  and onwards) the impact of Sn is of paramount importance. The rGO800-N based LIC, suffering from early lithium plating, performs poorly at high power rates compared to both Sn-containing LICs. Among them, the suitable mass balance of LIC2:1, ensuring the maximum performance of the negative electrode, leads to an improved energy to power performance at fast rates. In fact, LIC2:1 still retains an outstanding value of  $100 \text{ W h kg}^{-1}$  ( $25 \text{ W h L}^{-1}$ ) at  $5600 \text{ W kg}^{-1}$  and  $51 \text{ W h kg}^{-1}$  at its maximum power output  $25600 \text{ W kg}^{-1}$ . Fig. 5 also illustrates the improvement achieved with respect to previous studies reported by our group. It is clearly shown that from medium power density values and onwards LIC2:1 outperforms those described in ref. 22 and 23. It seems that the substitution of  $\text{SnO}_2$  by metallic Sn particles and nitrogen doping of the graphenic matrix is a good strategy for the design of anodes for high power performing LICs.

Owing to the excellent performance of LIC2:1, it was subjected to cycling stability tests at  $2 \text{ A g}^{-1}$  ( $t_{\text{discharge}} = 1 \text{ min}$ ). At this point, it is important to remember that one of the main challenges in LIC technology is keeping the cycling lifetime close to that of EDLCs. This is especially an issue for tin-based LICs suffering from huge volume expansions and subsequent pulverization accompanied by loss of electrical contact.<sup>19,22</sup> Herein, LIC2:1\_rGO800-N-Sn reaches 19 000 cycles with full

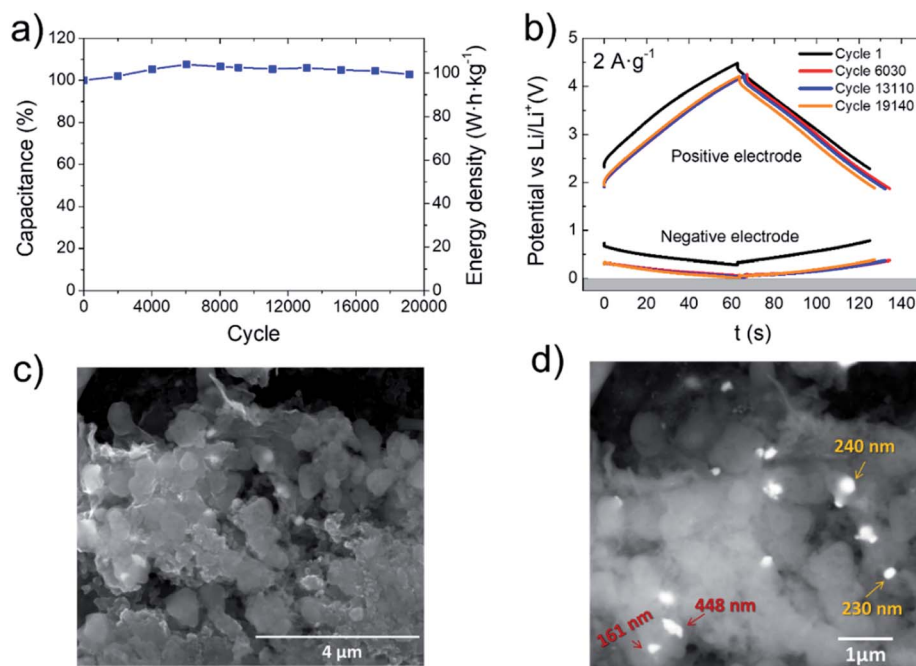


Fig. 6 Cycling performance of LIC2:1\_rGO800-N-Sn at  $2 \text{ A g}^{-1}$  (a), galvanostatic charge discharge profiles of cycle 1, 6030, 13 110 and 19 140 (b) and SEM images of the cycled negative electrode (c and d).





Table 3 Electrochemical performance of representative Sn-based lithium ion capacitors

Positive electrode	Negative electrode	LIC max. energy density (W h kg <sup>-1</sup> )	LIC max. power density (W kg <sup>-1</sup> )	LIC power density at 100 W h kg <sup>-1</sup>	Number of cycles (retention%)	Ref.
Activated reduced graphene oxide, 182 F g <sup>-1</sup> at 0.1 A g <sup>-1</sup>	SnO <sub>2</sub> -Reduced graphene oxide, 400 mA h g <sup>-1</sup> at 0.5 A g <sup>-1</sup>	186	10 000	1000	5000 (70%)	23
Activated carbon from olive pits, 120 mA h g <sup>-1</sup> at 0.1 A g <sup>-1</sup>	SnO <sub>2</sub> -Reduced graphene oxide, 600 mA h g <sup>-1</sup> at 0.1 A g <sup>-1</sup>	150	12 000	700	5000 (65%)	22
Biomass activated carbon, 115 mA h g <sup>-1</sup> at 0.3 A g <sup>-1</sup>	Sn-C with N-doping 1000 mA h g <sup>-1</sup> at 0.2 A g <sup>-1</sup>	196	24 375	10 000	5000 (70%)	24
B,N-Doped carbon, 90 mA h g <sup>-1</sup> at 0.1 A g <sup>-1</sup>	SnS <sub>2</sub> /reduced graphene oxide, 1198 mA h g <sup>-1</sup> at 0.1 A g <sup>-1</sup>	150	35 000	10 000	10 000 (90%)	42
Activated carbon, 122 mA h g <sup>-1</sup> at 0.1 A g <sup>-1</sup>	N/P codoped Sn-C nanofibers for anode, 881 mA h g <sup>-1</sup> at 0.2 A g <sup>-1</sup>	186	20 000	400	10 000 (83.7%)	46
Waste coffee grounds derived PCN, 44 mA h g <sup>-1</sup> at 0.1 A g <sup>-1</sup>	SnO <sub>2</sub> anchored in N-doped PCN nanosheets, 799 mA h g <sup>-1</sup> at 0.1 A g <sup>-1</sup>	138	53 000	10 000	5000 (67%)	43
Activated carbon YP-80F	Dual carbon layer@SnO/SnO <sub>2</sub> 902 mA h g <sup>-1</sup> at 1.4 A g <sup>-1</sup>	200	12 000	2000	3000 (94%)	47
Jackfruit skin derived activated carbon, 100 mA h g <sup>-1</sup> at 0.1 A g <sup>-1</sup>	Marine inspired SnO <sub>2</sub> nanorods, 695 at 0.1 A g <sup>-1</sup>	187	40 000	30 000	10 000 (80%)	44
<b>Activated graphene/carbon composite, 136 mA h g<sup>-1</sup> at 0.25 A g<sup>-1</sup></b>	<b>Sn/N-Reduced graphene oxide, 473 mA h g<sup>-1</sup> at 0.37 A g<sup>-1</sup></b>	<b>133</b>	<b>25.600</b>	<b>5600</b>	<b>19 000 (100%)</b>	<b>This work</b>

capacity retention, delivering *ca.* 100 W h kg<sup>-1</sup> at 5600 W kg<sup>-1</sup> (Fig. 6a). This is one of the best values reported so far for Sn-based LICs (Table 3) and is comparable to the cycle life of EDLCs. Herein, a huge improvement has been achieved since our previous studies ref. 22 and 23, not only regarding the power performance but also the stability. It must also be considered that studies included in Table 3 (ref. 24, 42, 43 and 44) reporting higher energy densities in the entire power range display worse capacitance retention against cycling. In the best case in terms of cyclability, ref. 43 (100 W h kg<sup>-1</sup> @ 10 000 W kg<sup>-1</sup>), after 10 000 cycles the capacitance drops to 90%. Furthermore, these studies not always provide the operating range of the negative electrode (especially at high currents), which does not rule out lithium plating in these systems.

A deeper analysis including electrochemistry as well as SEM imaging of cycled electrodes was performed to fully understand the good stability against cycling. Fig. 6a and b reveal that the capacitance increases during the first 6030 cycles until it reaches the maximum (107%) and the electrodes shifted to lower potentials. This can be explained by considering that a certain fraction of Li<sup>+</sup> ions is irreversibly trapped in large Sn particles during the first 6030 cycles. As a consequence, the negative electrode is increasingly lithiated and its potential *vs.* Li/Li<sup>+</sup> progressively approaches zero. It can be observed that during the first cycles, the negative electrode swings from 0.68 to 0.27 V, releasing less than 30% of its full capacity (see Fig. 3b and 6b). Beyond cycle 6030, voltage swing decreases from 0.32 to 0.03 V, releasing more than 40% of its full capacity (see Fig. 3b and 6b), and when large tin particles are not able to accommodate more lithium, they break down into smaller ones. Afterwards, the voltage windows of both negative and positive electrodes remain almost constant. It is worth

remarking that the positive electrode works in the 1.91–4.22 V potential range, avoiding electrolyte decomposition.<sup>45</sup> After 19 140 cycles, the negative electrode approaches 0 V and the capacitance retention decays to 103%. This can be related to the excessive accumulation of Li<sup>+</sup> into smaller tin particles. At this point, the cell was stopped and opened to perform post-cycling analysis before suffering from lithium plating. In good agreement with previous explanation, SEM images of the cycled electrode (Fig. 6c and d) reveal that small submicrometer-sized Sn particles have preserved their structure (Fig. 6c yellow arrows) while larger ones have been pulverized down to 150–500 nm size upon cycling (Fig. 6c red arrows). At this point, the N-doped graphene matrix is able to buffer volume changes, prevent loss of electrical contact and keep Sn particles highly active.

## 4. Conclusions

Novel composites comprising N-doped graphene and submicrometer-sized tin particles have been successfully prepared by a simple and low-cost synthetic route. Their potential as a battery-type electrode for lithium-ion capacitors was demonstrated. The small size of tin particles homogeneously embedded in the conducting N-graphene matrix allowed the electrode to reach high specific capacities even at high current rates (476 mA h g<sup>-1</sup> at C/10 and 120 mA h g<sup>-1</sup> at 10C). Full optimization of LICs through 2 : 1 positive to negative mass balance allowed an improvement of the performance at high current rates, delivering 133 W h kg<sup>-1</sup> at 142 W kg<sup>-1</sup> and 51 W h kg<sup>-1</sup> at a maximum of 25.600 W kg<sup>-1</sup>. Furthermore, LIC2:1 overcomes common tin based LIC stability issues showing full capacity retention after 19 000 cycles, which



corresponds to an energy delivery of  $100 \text{ W h kg}^{-1}$ . Deeper analysis revealed that during the first cycles, big tin particles were pulverized to smaller nanometric sizes. At this point, the N-graphene conductive matrix can buffer volume changes, allowing tin particles to remain highly active, and further improve the full cell cycling performance.

## Conflicts of interest

There are no conflicts to declare.

## Acknowledgements

The authors thank the European Union (Graphene Flagship, Core 3, Grant number 881603) and the Spanish Ministry of Science and Innovation (MICINN/FEDER) (RTI2018-096199-B-I00) for the financial support of this work. J. L. G. U. is very thankful to the Spanish Ministry of Education, Science and Universities (MICINN) for the FPU grant (16/03498). We also want to acknowledge the company GRAPHENEA for supplying the graphene oxide used in this work. María Etxebarria, María Jauregui and Diana Lopez are acknowledged for their assistance with the TEM, XRD and ICP measurements.

## References

- M. Li, J. Lu, Z. Chen and K. Amine, *Adv. Mater.*, 2018, **30**, 1800561.
- S. A. Hasib, S. Islam, R. K. Chakraborty, M. J. Ryan, D. K. Saha, M. H. Ahamed, S. I. Moyeen, S. K. Das, M. F. Ali, M. R. Islam, Z. Tasneem and F. R. Badal, *IEEE Access*, 2021, **9**, 86166–86193.
- S. Banerjee, B. De, P. Sinha, J. Cherusseri and K. K. Kar, in *Handbook of Nanocomposite Supercapacitor Materials I: Characteristics*, ed. K. K. Kar, Springer International Publishing, Cham, 2020, pp. 341–350.
- P. K. Sharma, A. Arora and S. K. Tripathi, *J. Energy Storage*, 2019, **21**, 801–825.
- B. Babu, P. Simon and A. Balducci, *Adv. Energy Mater.*, 2020, 2001128.
- J. J. Lamb and O. S. Burheim, *Energies*, 2021, **14**, 979.
- M. Soltani and S. H. Beheshti, *J. Energy Storage*, 2021, **34**, 102019.
- S. S. Zhang, *Batteries Supercaps*, 2020, **3**, 1137–1146.
- L. Li, D. Zhang, J. Deng, Y. Gou, J. Fang, H. Cui, C. Zhang and M. Cao, *Sustainable Energy Fuels*, 2021, **5**, 3278–3291.
- Z.-Y. Chen, B. He, D. Yan, X.-F. Yu and W.-C. Li, *J. Power Sources*, 2020, **472**, 228501.
- Y. Zheng, H. Wang, S. Sun, G. Lu, H. Liu, M. Huang, J. Shi, W. Liu and H. Li, *Sustainable Energy Fuels*, 2020, **4**, 1789–1800.
- H. Bi, X. Li, J. Chen, L. Zhang and L. Bie, *J. Mater. Sci.: Mater. Electron.*, 2020, **31**, 22224–22238.
- H. Mou, W. Xiao, C. Miao, R. Li and L. Yu, *Front. Chem.*, 2020, **8**, 141.
- R. Mo, X. Tan, F. Li, R. Tao, J. Xu, D. Kong, Z. Wang, B. Xu, X. Wang, C. Wang, J. Li, Y. Peng and Y. Lu, *Nat. Commun.*, 2020, **11**, 1374.
- C. Botas, D. Carriazo, G. Singh and T. Rojo, *J. Mater. Chem. A*, 2015, **3**, 13402–13410.
- J. Shan, Y. Liu, P. Liu, Y. Huang, Y. Su, D. Wu and X. Feng, *J. Mater. Chem. A*, 2015, **3**, 24148–24154.
- C. Tan, J. Cao, A. M. Khattak, F. Cai, B. Jiang, G. Yang and S. Hu, *J. Power Sources*, 2014, **270**, 28–33.
- X. Zhou, J. Bao, Z. Dai and Y.-G. Guo, *J. Phys. Chem. C*, 2013, **117**, 25367–25373.
- X. Zuo, B. Li, K. Chang, H. Tang and Z. Chang, *RSC Adv.*, 2017, **7**, 53126–53134.
- G. Moreno-Fernández, J. L. Gómez-Urbano, M. Enterría, T. Rojo and D. Carriazo, *J. Mater. Chem. A*, 2019, **7**, 14646–14655.
- G. Moreno-Fernández, M. Granados-Moreno, J. L. Gómez-Urbano and D. Carriazo, *Batteries Supercaps*, 2021, **4**, 469–478.
- M. Arnaiz, C. Botas, D. Carriazo, R. Mysyk, F. Mijangos, T. Rojo, J. Ajuria and E. Goikolea, *Electrochim. Acta*, 2018, **284**, 542–550.
- J. Ajuria, M. Arnaiz, C. Botas, D. Carriazo, R. Mysyk, T. Rojo, A. V. Talyzin and E. Goikolea, *J. Power Sources*, 2017, **363**, 422–427.
- F. Sun, J. Gao, Y. Zhu, X. Pi, L. Wang, X. Liu and Y. Qin, *Sci. Rep.*, 2017, **7**, 40990.
- M. Alaf, D. Gultekin and H. Akbulut, *Acta Phys. Pol., A*, 2013, **123**, 323–325.
- J.-F. Wang and D.-N. He, *Dalton Trans.*, 2018, **47**, 15307–15311.
- N. Jarulertwathana, V. Laokawee, W. Susingrat, S.-J. Hwang and T. Sarakonsri, *J. Mater. Sci.: Mater. Electron.*, 2017, **28**, 18994–19002.
- L. Liu, X. Huang, X. Guo, S. Mao and J. Chen, *J. Power Sources*, 2016, **328**, 482–491.
- A. Kovtun, D. Jones, S. Dell'Elce, E. Treossi, A. Liscio and V. Palermo, *Carbon*, 2019, **143**, 268–275.
- M. Scardamaglia, T. Susi, C. Struzzi, R. Snyders, G. Di Santo, L. Petaccia and C. Bittencourt, *Sci. Rep.*, 2017, **7**, 7960.
- R. Larciprete, P. Lacovig, S. Gardonio, A. Baraldi and S. Lizzit, *J. Phys. Chem. C*, 2012, **116**, 9900–9908.
- J. R. Pels, F. Kapteijn, J. A. Moulijn, Q. Zhu and K. M. Thomas, *Carbon*, 1995, **33**, 1641–1653.
- Y.-X. Yu, *Phys. Chem. Chem. Phys.*, 2013, **15**, 16819.
- L.-L. Tian, X.-Y. Wei, Q.-C. Zhuang, C.-H. Jiang, C. Wu, G.-Y. Ma, X. Zhao, Z.-M. Zong and S.-G. Sun, *Nanoscale*, 2014, **6**, 6075–6083.
- T. Hu, X. Sun, H. Sun, G. Xin, D. Shao, C. Liu and J. Lian, *Phys. Chem. Chem. Phys.*, 2014, **16**, 1060–1066.
- M. Thommes, K. Kaneko, A. V. Neimark, J. P. Olivier, F. Rodriguez-Reinoso, J. Rouquerol and K. S. W. Sing, *Pure Appl. Chem.*, 2015, **87**, 1051–1069.
- A. Wang, S. Kadam, H. Li, S. Shi and Y. Qi, *npj Comput. Mater.*, 2018, **4**, 15.
- Q. Sun, Y. Huang, S. Wu, Z. Gao, H. Liu, P. Hu and L. Qie, *Nanomaterials*, 2019, **9**, 1084.



- 39 M. Arnaiz and J. Ajuria, *Batteries Supercaps*, 2021, **4**, 733–748.
- 40 T. Panja, J. Ajuria, N. Díez, D. Bhattacharjya, E. Goikolea and D. Carriazo, *Sci. Rep.*, 2020, **10**, 10842.
- 41 U. Janakiraman, T. R. Garrick and M. E. Fortier, *J. Electrochem. Soc.*, 2020, **167**, 160552.
- 42 Y. Hao, S. Wang, Y. Shao, Y. Wu and S. Miao, *Adv. Energy Mater.*, 2020, **10**, 1902836.
- 43 C. Liu, Z. He, J. Niu, Q. Cheng, Z. Zhao, H. Li, J. Shi and H. Wang, *RSC Adv.*, 2021, **11**, 10018–10026.
- 44 P. Sennu, V. Aravindan and Y.-S. Lee, *Chem. Eng. J.*, 2017, **324**, 26–34.
- 45 B. Babu, C. Neumann, M. Enke, A. Lex-Balducci, A. Turchanin, U. S. Schubert and A. Balducci, *J. Power Sources*, 2021, **496**, 229797.
- 46 C. Yang, J. Ren, M. Zheng, M. Zhang, Z. Zhong, R. Liu, J. Huang, J. Lan, Y. Yu and X. Yang, *Electrochim. Acta*, 2020, **359**, 136898.
- 47 A.-Y. Kim, R. E. A. Ardhi, G. Liu, J. Y. Kim, H.-J. Shin, D. Byun and J. K. Lee, *Carbon*, 2019, **153**, 62–72.

